Available online at www.sciencedirect.com
ScienceDirect
Trans. Nonferrous Met. Soc. China 35(2025) 1182−1196
Transactions of Nonferrous Metals Society of China
www.tnmsc.cn

Microstructure evolution of K439B Ni-based superalloy casting with varying cross-sections by experiments and simulations

Da-shan SUI[1], De-peng ZHOU[1], Yang LIU[1], Yu SHAN[1], An-ping DONG[2]

1. Institute of Forming Technology & Equipment, School of Materials Science and Engineering, Shanghai Jiao Tong University, Shanghai 200030, China;
2. Shanghai Key Laboratory of Advanced High-temperature Materials and Precision Forming, School of Materials Science and Engineering, Shanghai Jiao Tong University, Shanghai 200240, China

Received 4 August 2023; accepted 2 April 2024

Abstract: Casting experiments and macro-micro numerical simulations were conducted to examine the microstructure characteristics of K439B nickel-based superalloy casting with varying cross-sections during the gravity investment casting process. Firstly, microstructure analysis was conducted on the casting using scanning electron microscopy (SEM) and electron backscatter diffraction (EBSD). Subsequently, calculation of the phase diagram and differential scanning calorimetry (DSC) tests were conducted to determine the macro-micro simulation parameters of the K439B alloy, and the cellular automaton finite element (CAFE) method was employed to develop macro-micro modeling of K439B nickel-based superalloy casting with varying cross-sections. The experimental results revealed that the ratio of the average grain area increased from the edge to the center of the sections as the ratio of the cross-sectional area increased. The simulation results indicated that the average grain area increased from 0.885 to 0.956 mm^2 as the ratio of the cross-sections increased from 6∶1 to 12∶1. The experiment and simulation results showed that the grain size became more heterogeneous and the grain shape became more irregular with an increase in the ratio of the cross-sectional area of the casting. CAFE modeling was an effective method to simulate the microstructure evolution of the K439B alloy and ensure the accuracy of the simulation.

Key words: K439B nickel-based superalloy; cellular automaton; cellular automaton finite element method; varying cross-section; investment casting; microstructure evolution

1 Introduction

Ni-based superalloys have a good combination of performance at high temperatures [1,2], making them widely used in hot-end components, such as aero-engines and gas turbines [3]. K439B is a nickel-based superalloy that has a temperature-bearing capacity of 800 °C. ZHANG et al [4] studied the effect of different pouring temperatures on the microstructure and mechanical properties of the alloy. Their findings indicated that increasing the pouring temperature appropriately is beneficial to improving the properties. ZHANG et al [5] studied the effect of hot isostatic treatment on the microstructure of the alloy casting and determined that hot isostatic treatment could effectively eliminate the microscopic shrinkage and reduce the elemental segregation. ZHENG et al [6] simulated the casting defects of K439B alloy by using a shrinkage criterion based on Darcy's law and optimized the gating system. CHEN et al [7] investigated the microstructure and properties of K439B after long-term aging at 800 °C. The study

Corresponding author: Da-shan SUI, Tel: +86-21-62933955, E-mail: dasui@sjtu.edu.cn;
An-ping DONG, Tel: +86-21-54742683, E-mail: apdong@sjtu.edu.cn
DOI: https://doi.org/10.1016/S1003-6326(24)66742-7

indicated that the alloy exhibited superior resistance to oxidation and corrosion compared to the K4169 alloy.

The cellular automaton (CA) method of microstructure simulation is widely employed due to its ability to easily couple with various physical fields, handle large computational domains, and achieve high efficiency [8]. Grain growth is influenced by heat, mass, and flow transfer, so microstructure simulation should be coupled with macroscopic physical fields [9,10]. RAPPAZ and GANDIN [11−13] first proposed a two-dimensional CA model based on the quasi-continuous nucleation model and KGT dendritic growth model. Then, many scholars studied the methods of coupling CA models with finite difference (FD) and finite element (FE) methods [14−17]. Some researchers studied the microstructure evolution using the CAFE method [18−21]. LU et al [22] established a two-dimensional model coupling Lattice Boltzmann (LB), CA, and FD methods to study the effect of wettability on dendritic growth during solidification. They found that wettability and cooling rate had a significant influence on the presence of bubbles in the microstructure.

In this work, investment casting experiments and macro-micro modeling were conducted for a K439B alloy casting with varying cross-sections. The effect of varying cross-sections on the microstructure evolution of K439B alloy was examined by comparing the experimental results with the corresponding simulation results. The study will provide a theoretical foundation for adjusting the microstructure of the K439B alloy.

2 Experimental

The raw material used in the casting experiments was the as-cast K439B nickel-based superalloy, supplied by Beijing Institute of Aeronautical Materials, China. The casting was designed with a cross-sectional area ratio of 6:1 (the ratio of the cross-sectional area of a thick rod with a diameter of 31 mm to a thin rod with a diameter of 12.5 mm) and 12:1 (the ratio of the cross-sectional area of a thick rod with a diameter of 44 mm to a thin rod with a diameter of 12.5 mm) to investigate the impact of varying cross-sections on microstructure evolution, as depicted in Figs. 1(a) and (b). The research focused on the microstructures in Regions A and B, as marked in Fig. 1(a).

The investment casting experiments were conducted. The mold shell was preheated to 850 °C and held for 3 h in a resistance furnace. 5 kg of K439B alloy was melted in a vacuum induction furnace. The preheated mold shell was placed in a vacuum chamber, and the pouring temperature was approximately 1500 °C. The prepared casting is shown in Fig. 1(c). Some specimens in Regions A and B were machined, ground, and corroded using a mixed solution with mass ratio of $CuSO_4$:HCl:H_2SO_4=30:100:7 and a corrosion time of 10 s. The microstructures of the specimens were analyzed using optical and scanning electron microscopy.

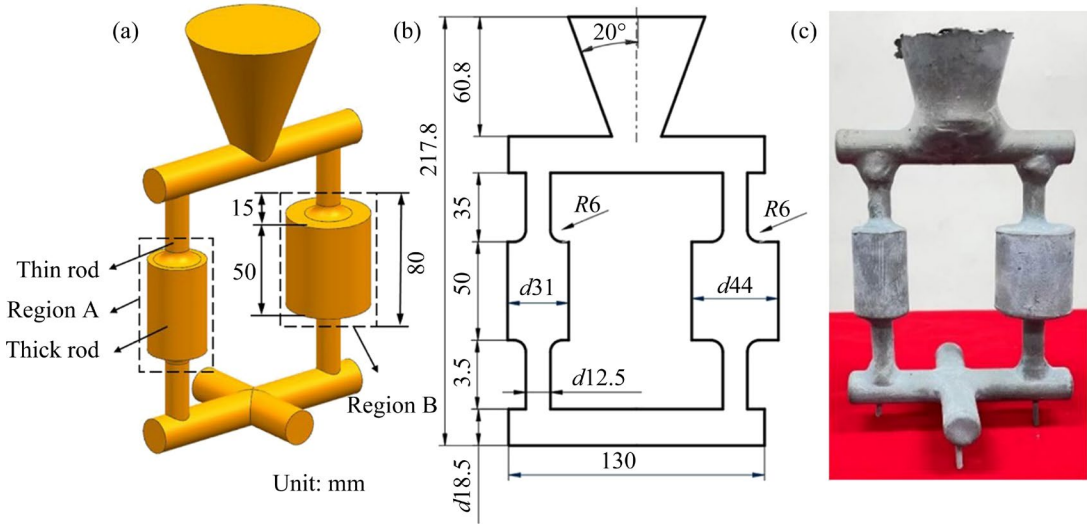

Fig. 1 Varying cross-sectional casting: (a) CAD model; (b) Drawing; (c) Prepared casting

3 Macro-micro numerical simulation

3.1 Finite element modeling

The finite element model was established by employing the casting simulation software, ProCAST, based on the CAD model, as shown in Fig. 1(a). The element sizes of the casting and mold shell were 1 and 2 mm, respectively. There are 1688935 tetrahedral elements in the casting.

According to the casting experiments, the simulation parameters were defined in detail. The pouring temperature of K438B was 1500 °C. The mold shell material was fused silica, with a thickness of 12 mm, and a preheating temperature was 850 °C. According to the software's database of boundary conditions, the interfacial heat transfer coefficient (IHTC) between the casting and mold shell was defined based on Ref. [23]. The heat transfer coefficient between the mold shell and the environment was 10 W/(m^2·K), and the radiation coefficient was 0.8.

3.2 Nucleation and growth models

Grain nucleation is typically considered as non-uniform nucleation. The nucleation model proposed by RAPPAZ and GANDIN [11] is used in this paper. This model describes the variation of nucleation density at different locations by utilizing a continuous distribution function, dn/d(ΔT). The expression is as follows:

$$\frac{\mathrm{d}n}{\mathrm{d}(\Delta T)}=\frac{n_{\max}}{\sqrt{2\pi}\Delta T_{\sigma}}\exp\left[-\frac{(\Delta T-\Delta T_{\max})^2}{2\Delta T_{\sigma}^2}\right] \tag{1}$$

where dn is the increase in nucleation density caused by the increase in the degree of supercooling, $n_{\max}$ is the maximum nucleation density, ΔT is the degree of supercooling, ΔT_{σ} is the standard deviation of the degree of supercooling, and $\Delta T_{\max}$ is the maximum degree of supercooling.

The nucleation density, $n(\Delta T)$, at a specific degree of supercooling, ΔT, can be determined by integrating the function in Eq. (1). The expression is as follows:

$$n(\Delta T)=\int_0^{\Delta T}\frac{\mathrm{d}n}{\mathrm{d}(\Delta T)}\mathrm{d}(\Delta T) \tag{2}$$

The nucleation conditions are different between the surface and interior of the casting during the crystallization process, and the Gaussian distribution of the nucleation parameters is also different [11].

According to the solidification theory, grain growth is driven by the degree of supercooling at the dendrite front, and it is expressed as follows [9]:

$$\Delta T=\Delta T_{\mathrm{c}}+\Delta T_{\mathrm{t}}+\Delta T_{\mathrm{r}}+\Delta T_{\mathrm{k}} \tag{3}$$

where ΔT_{c} represents the compositional degree of supercooling, ΔT_{t} represents the thermodynamic degree of supercooling, ΔT_{r} represents the curvature degree of supercooling, and ΔT_{k} represents the kinetic degree of supercooling. For most alloys, degrees of supercooling other than the compositional one can be neglected, which means $\Delta T\approx\Delta T_{\mathrm{c}}$. Under these conditions, the KGT model [24] could be used to analyze the growth of columnar and equiaxed grains. The relationship between the growth rate of the dendrite tip, v, and the degree of supercooling is simplified as follows:

$$v=a_2\Delta T^2+a_3\Delta T^3 \tag{4}$$

where a_2 (m/(s·K^2)) and a_3 (m/(s·K^3)) are the growth kinetic parameters, respectively, and they are constants associated with the alloy.

The KGT model is typically applicable to binary alloys. The equivalent method is used for multicomponent alloys, and the initial concentration (c_0), the slope of the liquid phase line (m), and the solute equilibrium partition coefficient (k) are calculated as follows:

$$c_0=\sum c_i \tag{5}$$

$$m=\frac{\sum(m_i c_i)}{c_0} \tag{6}$$

$$k=\frac{\sum(m_i c_i k_i)}{m c_0} \tag{7}$$

where c_i, m_i, and k_i represent the mass fraction, the slope of the liquid phase line, and the solute equilibrium partition coefficient of binary alloys, respectively. Therein, c_i was determined, and m_i and k_i were calculated using the calculation of the phase diagram (CALPHAD).

3.3 Parameters determination

The cooling rate of the alloy in the real casting process is typically around 0.83−1.67 °C/s. Thus,

back diffusion was selected as the solid phase diffusion model. Meanwhile, the CALPHAD analysis of the K439B alloy was conducted using the CALPHAD module in ProCAST. The solidus and liquidus temperatures of the K439B alloy were determined to be 1235 and 1314 °C, respectively. The slope of the liquid phase line, m, the solute equilibrium partition coefficient, k, and the diffusion coefficient, D_1, were also calculated. Some of the results are listed in Table 1.

Table 1 Calculation results of CALPHAD

Element	Liquidus slope, m	Average distribution coefficient of solute, k	Diffusion coefficient, D_1/(m^2·s^{-1})
Al	−5.0443	1.2238	3×10^{-9}
C	−36.8495	0.1133	3×10^{-9}
Co	0.1069	1.0721	3×10^{-9}
Cr	−5.2233	0.9174	3×10^{-9}
Nb	−9.9523	0.5016	3×10^{-9}
Ti	−16.4569	0.6153	3×10^{-9}
W	−2.9446	0.8925	3×10^{-9}

The growth kinetic coefficients were also calculated based on the results of the CALPHAD module in ProCAST. The results are as follows: a_2= 1.420912×10^{-7} m/(s·K^2); a_3=9.528034×10^{-7} m/(s·K^3).

It is difficult to measure the nucleation parameters through experiments, and these parameters also vary widely across different processes. Thus, the magnitudes of nucleation parameters were determined according to the methods in Refs. [21,25,26,27]. Then, the algorithm recommended by the ASTM standard was used.

$$N_V=0.8N_S^{3/2}=0.5659N_L^3 \tag{8}$$

where N_V, N_S, and N_L represent the number of nuclei per unit volume, per surface area, and per line length, respectively.

The numbers of nuclei in terms of volume and area were determined by analyzing the grain distribution using EBSD image depicted in Fig. 2. The results are summarized in Table 2. The volume parameters of nuclei were primarily considered as they have a greater impact on the microstructure simulation compared to the area parameters of nuclei.

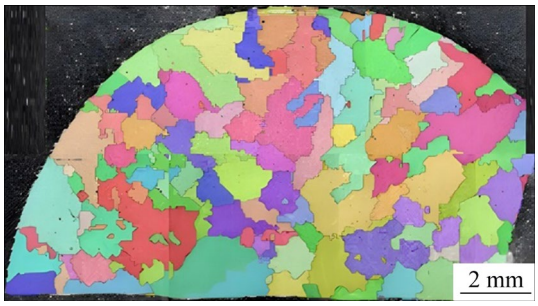

Fig. 2 EBSD image in local region of casting

Table 2 Nucleation parameters in Regions A and B in Fig. 1(a)

Region	$N_{V,max}$/ m^{-3}	$\Delta T_{V,max}$/ K	$\Delta T_{V,\sigma}$/ K	$N_{S,max}$/ m^{-2}	$\Delta T_{S,max}$/ K	$\Delta T_{S,\sigma}$/ K
A	1.5×10^9	15	5	1.52×10^6	10	5
B	1.8×10^9	15	10	1.72×10^6	10	5

4 Results and discussion

4.1 Experimental results

4.1.1 Dendrite morphology

The dendrite morphologies in Regions A and B in Fig. 1(a) are shown in Figs. 3 and 4, respectively. The primary dendrite arm spacing (PDAS) was calculated, and the values were approximately 138−250 μm in Region A and 143−280 μm in Region B. According to solidification theory, the faster the cooling rate, the smaller the PDAS and the denser the microstructure under typical casting process conditions. Heat transfer speed in Region B was slower than that in Region A because the wall thickness in Region B is greater than that in Region A. Thus, the PDAS in Region B is larger. The experimental results are consistent with the corresponding theory of solidification.

It can be analyzed from Figs. 3 and 4 that the directions of grain growth are clear and distinguishable at various locations in Regions A and B. At the top (location a) and bottom (location c), the grains on the edges mainly grew in the direction pointing towards the center, as illustrated in Figs. 3(a), 3(c), 4(a), and 4(c). While in the middle (location b), the grains on the edges grew in the direction pointing towards the center, and the grains in the center grew non-directionally, as shown in Figs. 3(b) and 4(b). According to solidification theory, the growth direction of grains

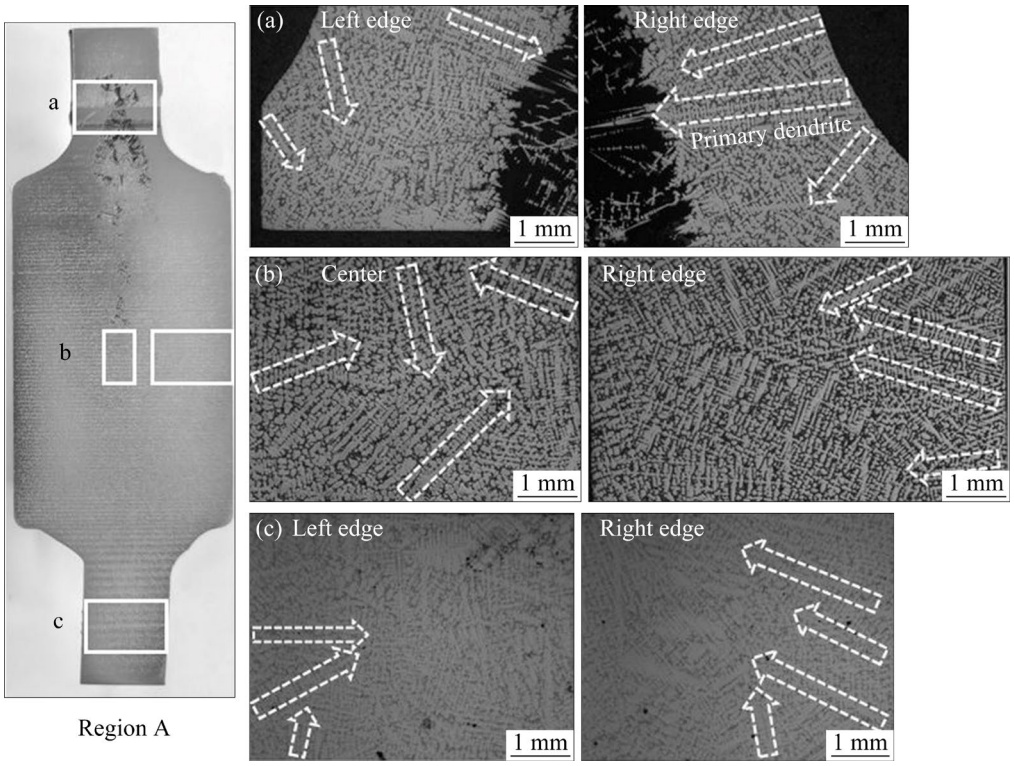

Fig. 3 Dendrite morphologies of Region A in Fig. 1(a): (a) Top; (b) Middle; (c) Bottom

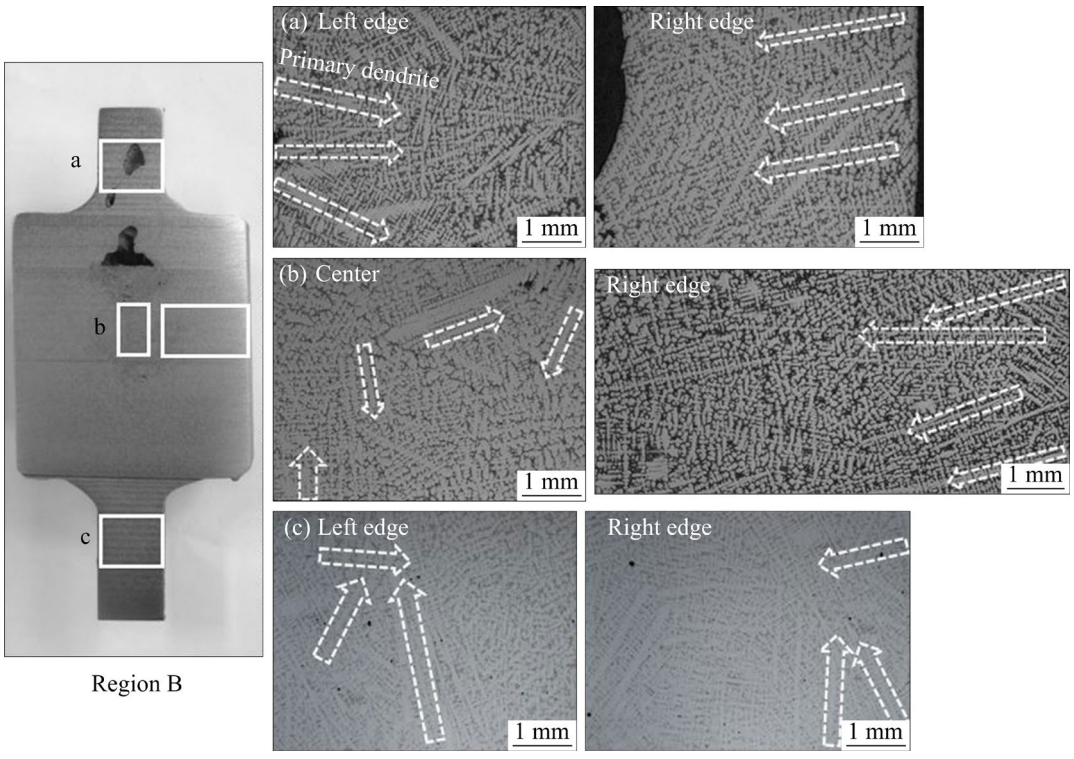

Fig. 4 Dendrite morphologies of Region B in Fig. 1(a): (a) Top; (b) Middle; (c) Bottom

is the characteristic by being along the direction of the inverse temperature gradient. The temperature gradients illustrate the variations from the innermost to the outermost regions and from smaller to larger sections. Therefore, the grains in Regions A and B exhibit the main characteristics of growing both vertically along the wall and pointing towards the center of the large Section b.

4.1.2 Solidification microstructure

Solidification microstructure typically consists of three regions in a casting, namely the surficial fine-grain region, the columnar-grain region, and the central equiaxed-grain region, arranged from the surface to the center. The microstructures of the specimens taken from Regions A and B in Fig. 1(a) are shown in Figs. 5 and 6, respectively, and the statistical curves related to grains are shown in Fig. 7. Cross-sections of Regions A and B reveal the presence of diffuse porosity, as depicted in Figs. 5(a), 6(a) and 6(b).

Compared to the microstructures in Sections a and b, f and g of Regions A and B, respectively, it is evident that the proportion of columnar-grain area in the microstructure decreases in Sections b and f, compared to Sections a and g. However, the columnar-to-equiaxed transition (CET) region and equiaxed grain area proportion increase in Sections b and f, as shown in Figs. 5(a), 5(b), 5(f), 5(g), 6(a), 6(b), 6(f) and 6(g). Moreover, the features in Region B are more distinguished than those in Region A.

Compared to the microstructures in Sections c, d and e of Regions A and B, respectively, it can be concluded that the proportion of columnar-grain area in the microstructure in Section d is smaller, while the proportion of equiaxed grain area is larger

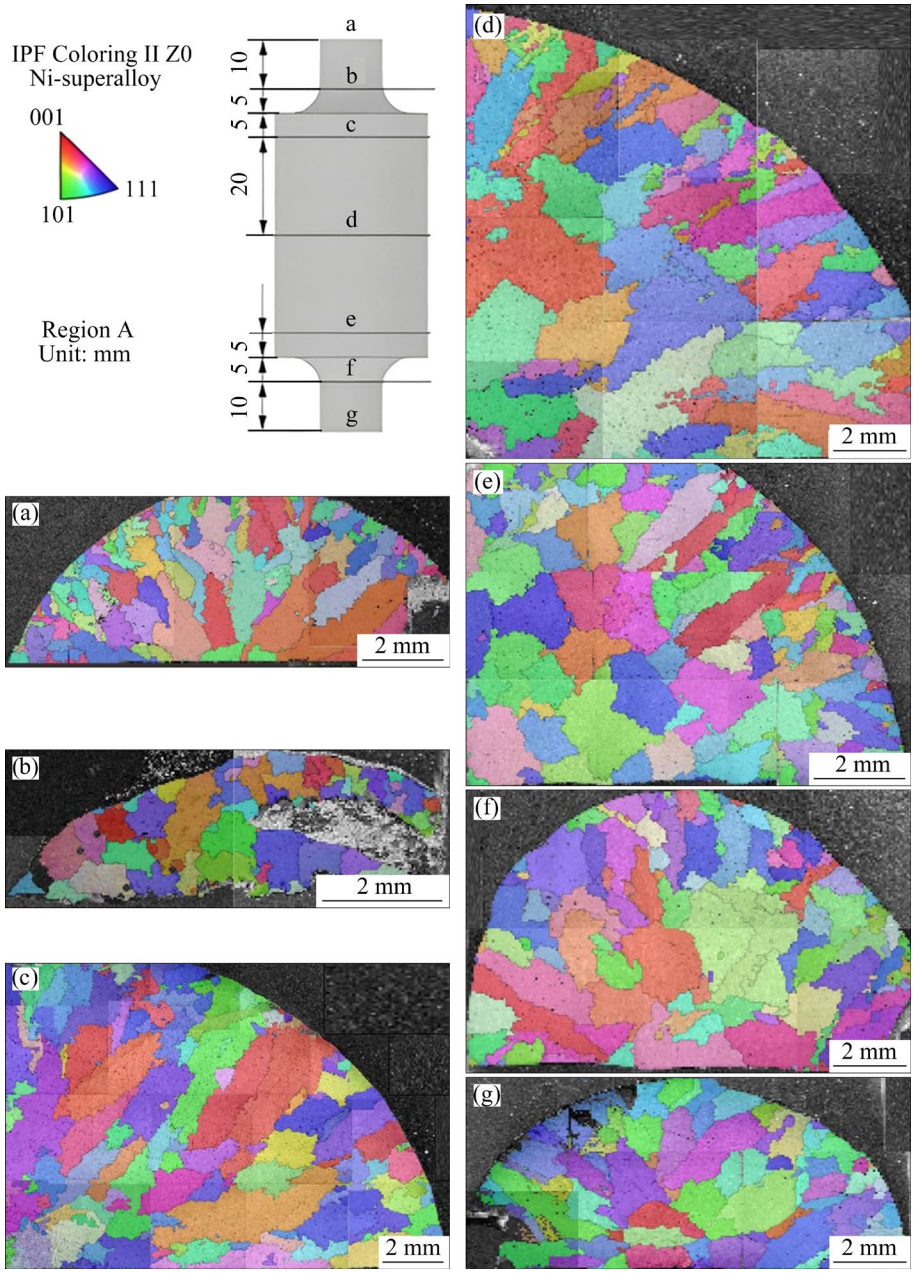

Fig. 5 EBSD results of cross-sections in Region A in Fig. 1(a)

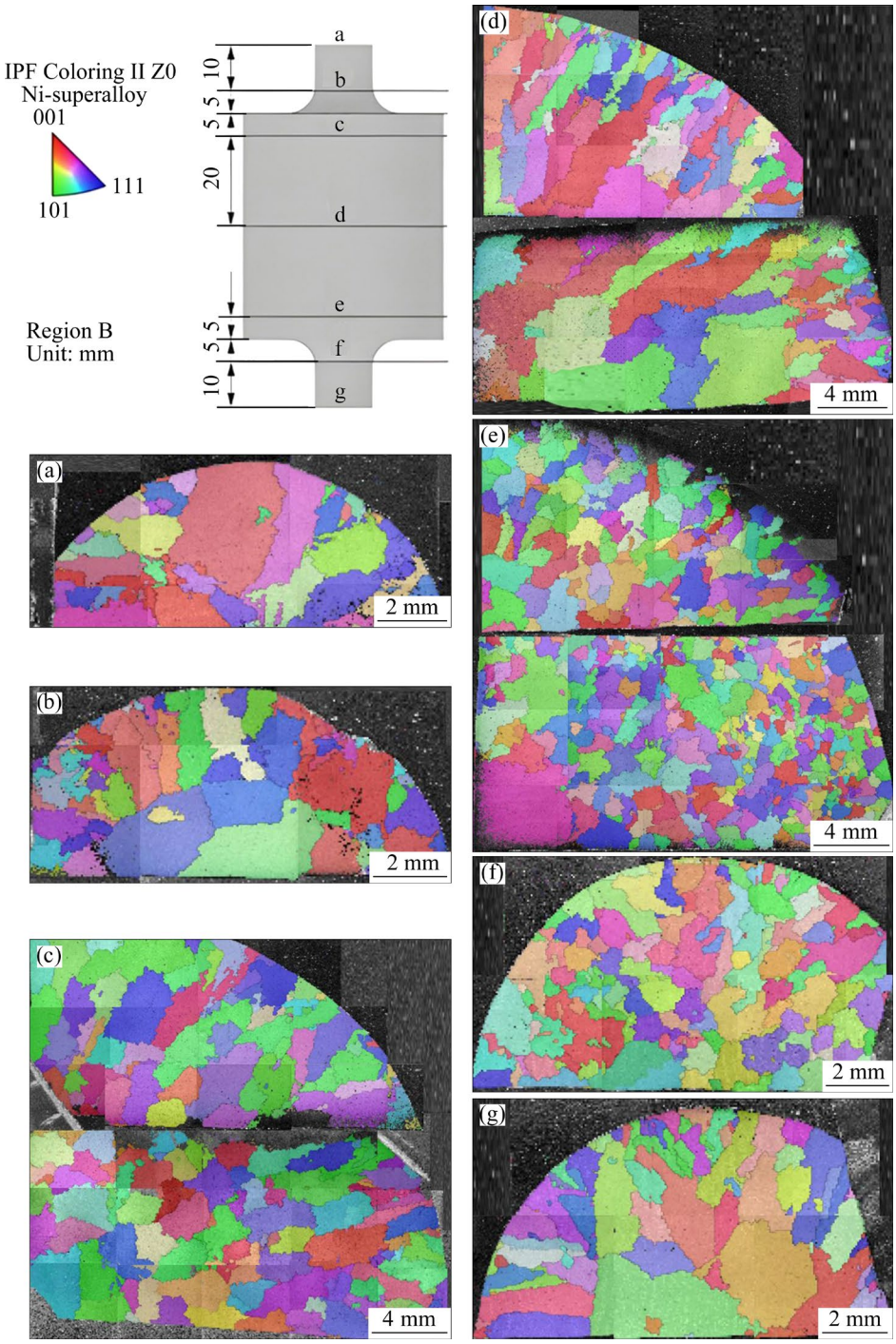

Fig. 6 EBSD results of cross-sections in Region B in Fig. 1(a)

than those in Sections c and e. However, due to the slow solidification speed in the center of Section d, the grains continue to grow for a long period at high temperatures, resulting in coarser grains, as shown in Figs. 5(c), 5(d), 5(e), 6(c), 6(d) and 6(e).

The average grain area in the center of the thick rod in Region B is approximately 1.206 mm^2, as shown in Section d of Fig. 6. The average grain area in Sections c and e is about 0.6 mm^2. The ratio of the average grain area in the center to the side is approximately 2:1. The difference in grain size between the center and side increased as the ratio of varying cross-sections increased, in comparison to the grain areas in Regions A and B.

There is no significant difference in the microstructure distribution between Sections b and c, and between Sections e and f, at the transition from a thin rod to a thick rod in Regions A and B.

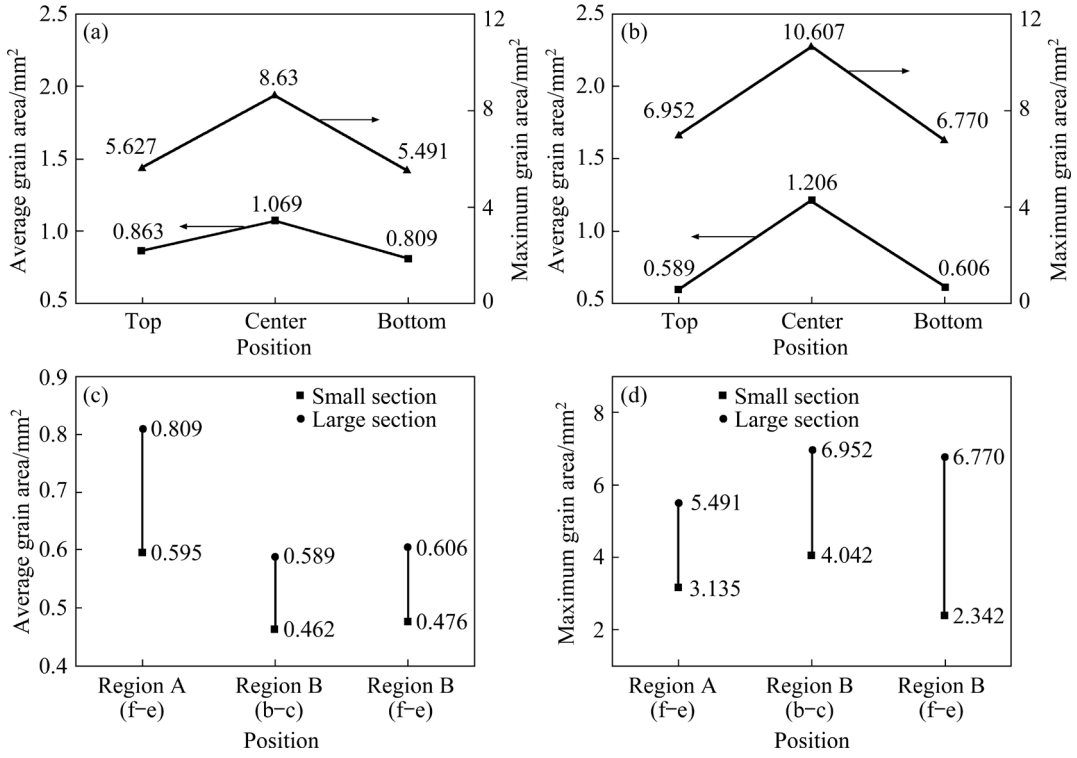

Fig. 7 Statistical curves of microstructures: (a) Large-section rod in Region A in Fig. 1(a); (b) Large-section rod in Region B in Fig. 1(a); (c) Average grain area at transition; (d) Maximum grain area at transition

But the average grain area hardly changed, while the maximum grain area increased significantly on the cross-sections from Sections b to c and from Sections f to e. This characteristic of the microstructure distribution is more pronounced in Region B compared to Region A. It can be observed that the center-to-edge ratios of the average grain areas in Regions A and B were approximately 5∶4 (1.069:0.809) and 2∶1 (1.206:0.606), respectively based on the experiment results shown in Fig. 7(a) and (b). And the average grain area on Sections b and c in Region B increases from 0.462 to 0.589 mm^2, representing a 27.5% increase, shown in Fig. 7(c). Additionally, the maximum grain area increases from 4.042 to 6.952 mm^2, indicating a 72% increase compared to the microstructure between Sections b and c in Region B, shown in Fig. 7(d). The reason is that the slower cooling rate of the molten alloy on the larger cross-section results in higher superheat and a larger temperature gradient. It is more conducive to speeding up columnar grain growth and promoting grain coarsening. Moreover, the larger the characteristic sizes of the varying cross-sections are, the more pronounced the effect of grain coarsening becomes. This implies that the largest grain area will be larger.

4.2 Simulation results of macroscopic fields

The simulation results of the temperature fields are shown in Fig. 8 at different fractions of solid (FS) during the solidification process. According to Fig. 8, the temperature of the thick rod in Region A gradually decreases from the outer to the inner of the casting, below the liquidus temperature of 1314 °C, when the FS is 12%. The temperature of the thick rod in Region B gradually decreases below the liquidus temperature from the outer to the inner when the FS is 25%. The temperatures of the thick rods in Regions A and B are lower than the solidus temperature, which is 1235 °C, when the FS is 37% and 61%, respectively. The casting temperature decreases below the solidus temperature completely when the FS reaches 82%.

The cooling rate significantly affects the nucleation and growth of grains during the solidification process. The average cooling rate is expressed as follows:

$$L=\left|\frac{T_{\text{upper}}-T_{\text{lower}}}{t_{\text{upper}}-t_{\text{lower}}}\right| \tag{9}$$

where L is the average cooling rate; T_{upper} and T_{lower}

represent the upper and lower limits of temperature calculation, which are the liquidus temperature of 1314 °C and the solidus temperature of 1235 °C, respectively; t_{upper} and t_{lower} represent the time taking for nodes in the calculation domain to reach the liquidus and solidus temperatures, respectively, and the difference between them is the time that takes for the temperature to change from the liquidus to the solidus.

The simulation results for the average cooling rate in the characteristic regions are shown in Fig. 9. There is no significant difference in the cooling rate of the thin rods between Regions A and B in Fig. 1(a). The cooling rate on the middle sections of both thin rods is approximately 4.74 °C/s in Region A and 4.72 °C/s in Region B. The cooling rate on the middle section of the thick rod is lower than that at the upper and lower ends in both regions. In Region A, the cooling rate at the center is approximately 0.88 °C/s, whereas at the lower end it is around 1.2 °C/s. The cooling rate of the thick rod in Region B is lower than that in Region A. This implies that increasing the cooling rate could promote grain refinement and result in a denser microstructure.

4.3 Simulation results of microstructure

The microstructure evolution of the K439B alloy casting was simulated using the CAFE method. The simulation results in Regions A and B are shown in Figs. 10 and 11, respectively. The statistical curves of grain area and shape factor on the longitudinal sections of Regions A and B in Fig. 1(a) are shown in Fig. 12. The shape factor represents the degree of sphericity of the grains, and a value closer to 1.0 indicates a more spherical shape (or a circular shape on the 2D section).

According to Figs. 10 and 11, a film of the fine-grain region was first formed on the casting surface because the high undercooling degree promoted grain nucleation close to the mold shell. Subsequently, grains that had already nucleated

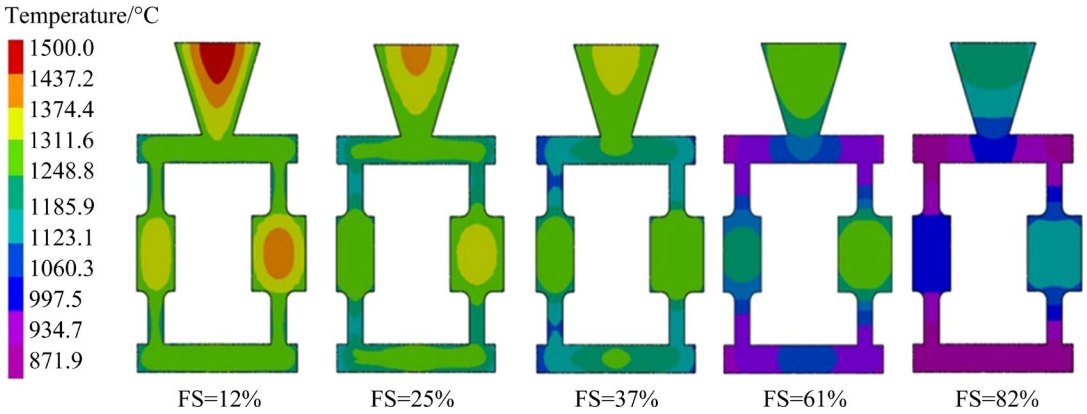

Fig. 8 Temperature fields during solidification

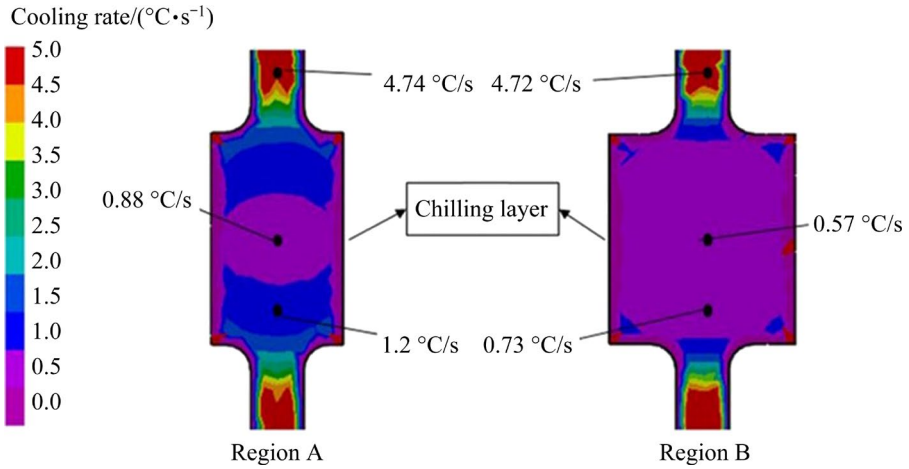

Fig. 9 Distribution of average cooling rate during solidification process

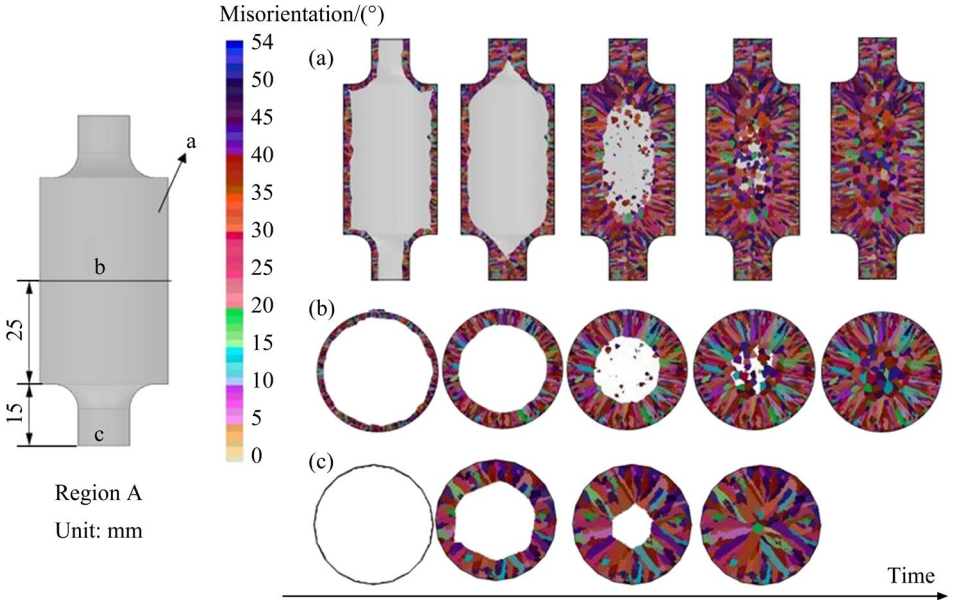

Fig. 10 Simulation results of microstructures in Region A in Fig. 1(a): (a) Longitudinal Section a; (b) Cross-section b; (c) Cross-section c

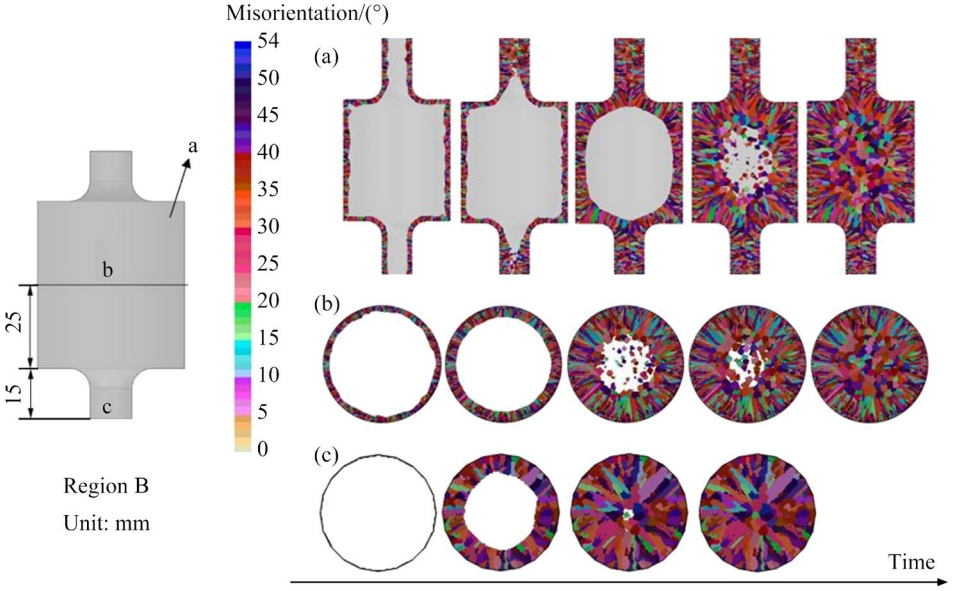

Fig. 11 Simulation results of microstructures in Region B in Fig. 1(a): (a) Longitudinal Section a; (b) Cross-section b; (c) Cross-section c

along the direction of the temperature gradient grew into columnar grains. As the columnar grains grew, solute enrichment occurred at the grain boundary. When the solute enrichment reached a critical value, free grains began to nucleate. This nucleation process restricted the growth of columnar grains and led to the formation of a transition region from columnar to equiaxed grains, known as the columnar-to-equiaxed transition (CET). Then, the region of equiaxed grains was formed after the nucleation and growth of grains in the center of the section.

Compared with Figs. 10(a) and 11(a), the grains grew along the direction of a temperature gradient that was inverse to the surface-to-center direction during microstructure evolution on the longitudinal section. Therefore, the distribution of equiaxed grains tended to be elliptical. The larger the section variation was, the more circular the distribution of the equiaxed grains region became.

In Region B where there was a significant variation in section thickness, the columnar grains were still in the growth stage in the thick rod, while

the microstructure evolution had already completed in the thin rod. In Region A, the grains were predominantly columnar in shape, and numerous free nuclei began to nucleate and grow at the center.

Compared with Figs. 10(b), 10(c), and 11(b), 11(c), the equiaxed-grain region was more distinct on Section b than on Section c of Regions A and B. This was a result of the smaller temperature gradient on Section b compared to Section c, which hindered the growth of columnar grains and allowed for ample space and time for nucleation and growth of free nuclei in the center. As a result, a more distinct equiaxed-grain region was formed.

Based on the statistical results shown in Fig. 12, both Regions A and B in Fig. 1(a) exhibit the phenomenon of small-sized grain aggregation, where grains with an area of 1 mm^2 account for more than 70%. The average grain area in Region B (0.956 mm^2) and its shape factor (2.927) are larger than those in Region A, which has an average grain area of 0.885 mm^2 and a shape factor of 2.879. The larger average grain area in Region B is due to its larger volume and poorer heat transfer conditions, which result in a prolonged high-temperature maintenance of the molten alloy and lead to grain coarsening. The larger shape factor in Region B is induced by its larger cross-section, which provides sufficient space for columnar grain growth before nucleation and growth in the center. This results in the formation of long and thin columnar grains.

4.4 Comparison of experiment and simulation results

According to the theory of alloy solidification, the growth direction of grains at rough interfaces is dependent on the direction of heat flow. The growth orientation of superalloys depends on the competition between the thermal orientation and the preferential orientation along the ⟨001⟩ direction. Moreover, preferential orientation plays a dominant role due to the relatively high growth rate with dendritic morphology [28].

The comparison of the experiment and simulation results of the microstructures on Sections a, b and c of Regions A and B in Fig. 1(a) is shown in Figs. 13 and 14, respectively. The growth direction

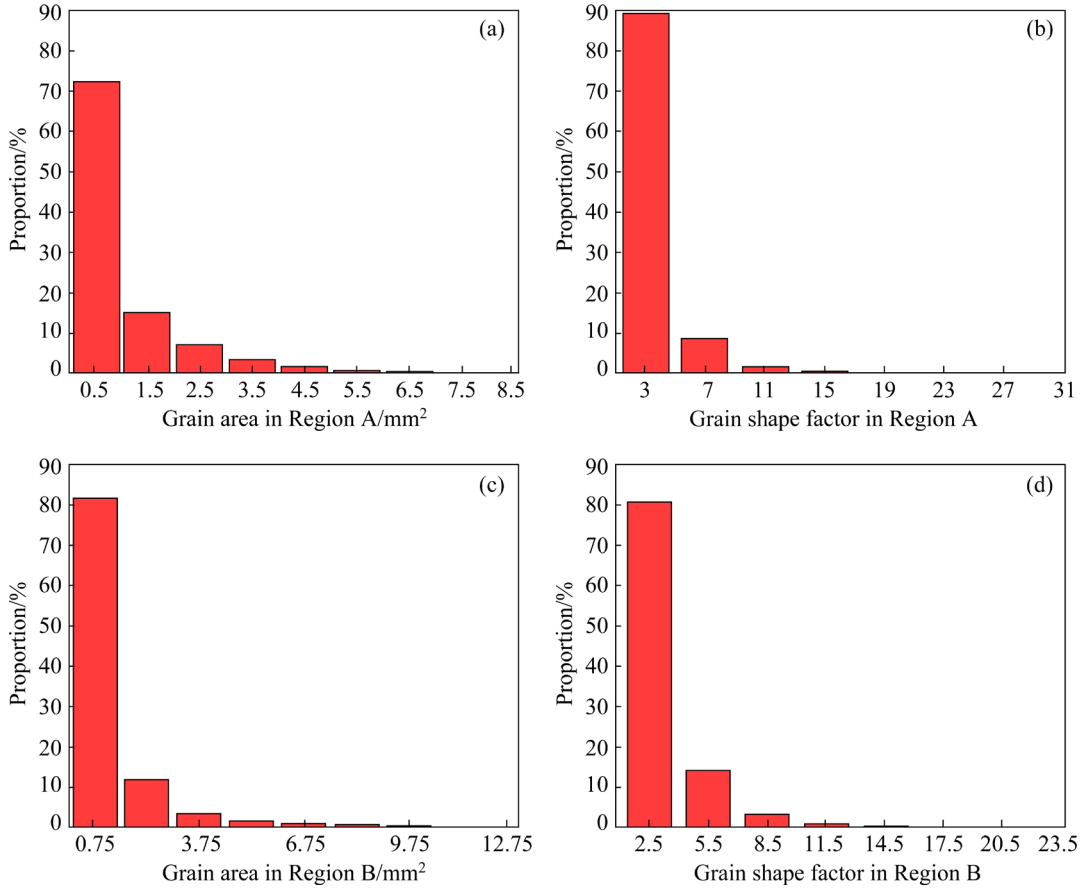

Fig. 12 Statistic results of grain area and shape factor on longitudinal section in Regions A and B in Fig. 1(a): (a) Grain area in Region A; (b) Grain shape factor in Region A; (c) Grain area in Region B; (d) Grain shape factor in Region B

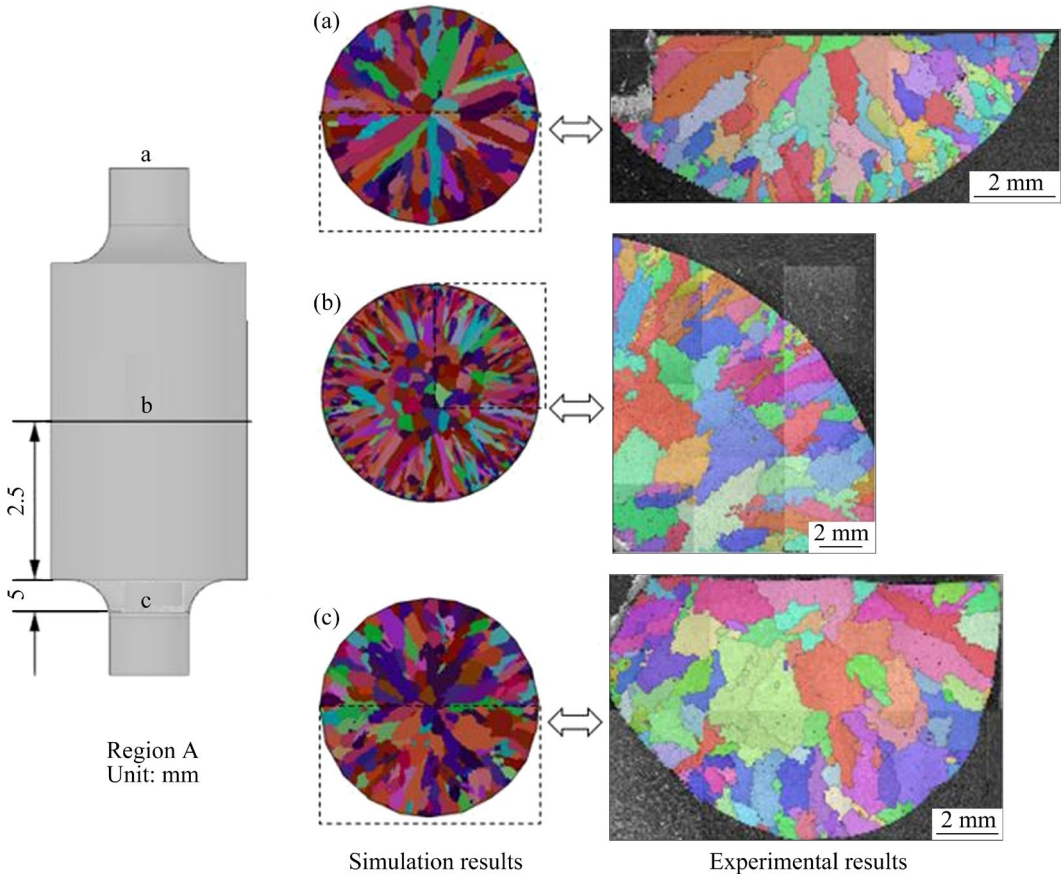

Fig. 13 Comparison of experiment and simulation results of microstructures in Region A in Fig. 1(a): (a) Cross-section a; (b) Cross-section b; (c) Cross-section c

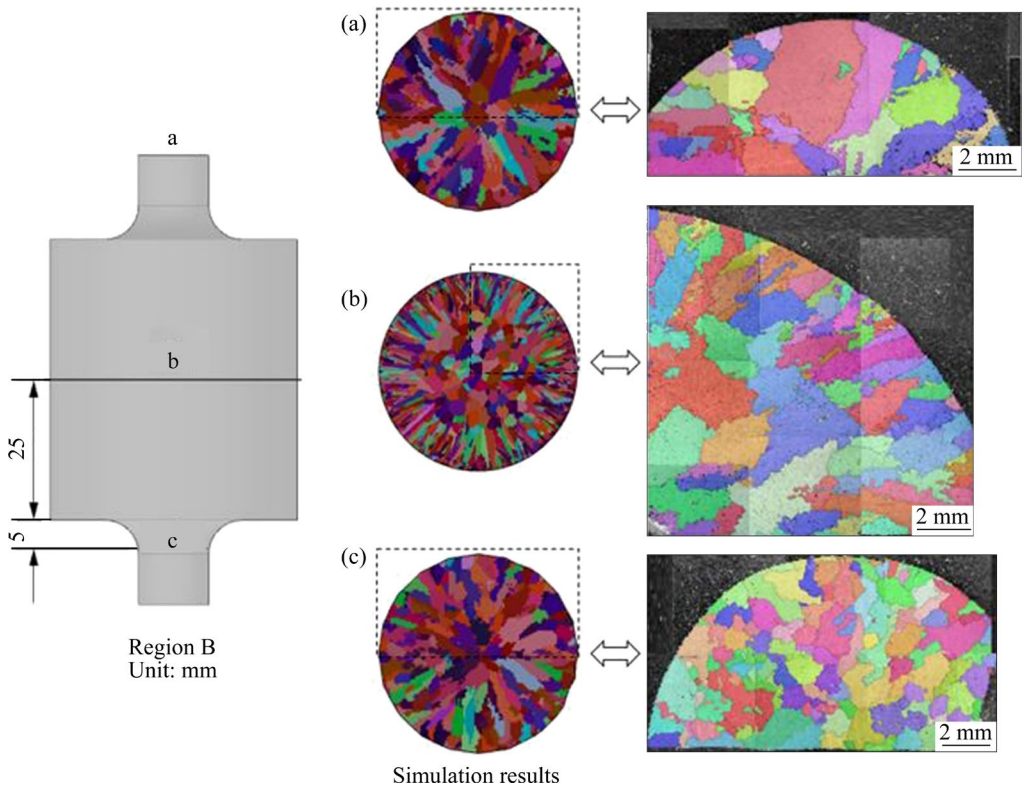

Fig. 14 Comparison of experiment and simulation results of microstructures in Region B in Fig. 1(a): (a) Cross-section a; (b) Cross-section b; (c) Cross-section c

of grains conforms to the theory of alloy solidification. Moreover, the simulation results for grain distribution, orientation and grain area are in good agreement with the experiment results. Specifically, both the experiment and simulation microstructures consist of a surficial fine-grain region, an intermediate columnar-grain region and a central equiaxed-grain region. Compared to the small Cross-sections a and c, the growth of columnar grains in the larger Section b is limited by the temperature gradient. This limitation leads to a relatively large proportion of the equiaxed-grain region. Combined with Table 3, the simulation errors for the average grain area are mostly less than 6.2%, except for a 14.5% error on Section a in Region A. This indicates that some improvements are needed in the macro-micro numerical modeling to further enhance the accuracy of the simulation.

Table 3 Comparison of experimental and simulation results of average grain area

Region	Section	Average grain area/mm^2		Error/%
		Simulation	Experiment	
A	a	0.601	0.525	14.5
	b	1.022	1.069	4.4
	c	0.558	0.595	6.2
B	a	0.521	0.493	5.7
	b	1.249	1.206	3.6
	c	0.489	0.476	2.7

5 Conclusions

(1) Based on the experiment results, the center-to-edge ratios of the average grain areas in Regions A and B for the K439B superalloy casting with varying cross-sections were approximately 5∶4 and 2∶1, respectively. The results indicated that the larger the sectional ratio of the varying cross-sectional casting, the greater the difference in the average grain area, resulting in more heterogeneous grains.

(2) Based on the macro-micro simulation results, as the sectional ratio of the casting increased from 6∶1 in Region A to 12∶1 in Region B, the columnar grains grew longer and thinner in the larger cross-sectional Region B compared to Region A. The average grain area in Region B was 0.956 mm^2, which was larger than the corresponding value of 0.885 mm^2 in Region A. Similarly, the shape factor in Region B was 2.927, which was greater than the corresponding value of 2.879 in Region A. These results indicated that the grains in Region B were more heterogeneous because of their larger sectional ratio.

(3) The comparison of experiment and simulation results revealed that the simulation errors for the average grain area were generally below 6.2%. The study also showed that CAFE model could be used to effectively simulate the microstructure evolution of the K439B alloy and ensure the accuracy of the simulation.

CRediT authorship contribution statement

Da-shan SUI: Investigation, Resources, Writing – Original draft preparation, Writing – Review and editing, Supervision; **De-peng ZHOU** and **Yang LIU:** Investigation, Writing – Original draft preparation; **Yu SHAN:** Investigation, Resources, Writing – Original draft preparation; **An-ping DONG:** Investigation, Resources, Writing – Review and editing, Supervision.

Declaration of competing interest

The authors declare that they have no known competing financial interests or personal relationships that could have appeared to influence the work reported in this paper.

Acknowledgments

This research was supported by the National Science and Technology Major Project of China (No. J2019-VI-0004-0117).

References

[1] JIANG Ju-fu, XIAO Guan-fei, WANG Ying, LIU Ying-ze, ZHANG Ying. High temperature deformation behavior and microstructure evolution of wrought nickel-based superalloy GH4037 in solid and semi-solid states [J]. Transactions of Nonferrous Metals Society of China, 2020, 30: 710−726.

[2] HAO Xin, LIU Guo-huai, WANG Ye, WU Shi-ping, WANG Zhao-dong. Optimization of investment casting process for K477 superalloy aero-engine turbine nozzle by simulation and experiment [J]. China Foundry, 2022, 19(4): 351−358.

[3] WHITMORE L, AHMADI M R, GUETAZ L, LEITNER H, ERWIN P K, STOCKINGER M, KIZESCHNIK E. The microstructure of heat-treated nickel-based superalloy 718Plus [J]. Materials Science and Engineering A, 2014, 610: 39−45.

[4] ZHANG Lei-lei, CHEN Jing-yang, QIAN lei, ZHANG Ming-jun, TANG Xin, YANG Qing. Effect of casting temperature on microstructure and mechanical properties of K439B superalloy [J]. Transactions of Materials and Heat

Treatment, 2019, 40(9): 57−63. (in Chinese)

[5] ZHANG Ming-jun, ZHANG Lei-lei, HU Ying-tao, TANG Xin, YANG Qing. Effect of hot isostatic pressing on microstructure of K439B superalloy [J]. Heat Treatment of Metals, 2020, 45(11): 177−181. (in Chinese)

[6] ZHENG Bo-yuan, WU Yi-dong, CHEN Jing-yang, XIAO Cheng-bo, LI Zong-zhen, HUI Xi-dong. Predication of the defects and optimization of the technology for the investment casting of thin-wall experimental cartridge receiver made of K439B superalloy [J]. Foundry Technology, 2023, 44(2): 147−152. (in Chinese)

[7] CHEN Jing-yang, REN Xiao-dong, ZHANG Ming-jun, ZHANG Li-hui, TANG Xin, XIAO Cheng-bo. Microstructure and typical properties of cast Ni-based superalloy K439B [J]. Heat Treatment of Metals, 2023, 48(1): 100−104. (in Chinese)

[8] WANG Jin-long, WANG Fu-ming, ZHAO Yan-yu, ZHANG Jiong-ming, REN Wei. Numerical simulation of 3D-microstructures in solidification processes based on the CAFE method [J]. International Journal of Minerals, Metallurgy and Materials, 2009, 16(6): 640−645.

[9] SALUJA R S, GANESH NARAYANAN R, DAS S. Cellular automata finite element (CAFE) model to predict the forming of friction stir welded blanks [J]. Computational Materials Science, 2012, 58: 87−100.

[10] JING Cai-liang, XU Zhi-gang, WANG Ying, WANG Wan-jun. Simulation on solidification structure of 72A tire cord steel billet using CAFE method [J]. China Foundry, 2012, 9(1): 53−59.

[11] RAPPAZ M, GANDIN C A. Probabilistic modelling of microstructure formation in solidification processes [J]. Acta Metallurgica et Materialia, 1993, 41(2): 345−360.

[12] GANDIN C A, RAPPAZ M. A coupled finite element-cellular automaton model for the prediction of dendritic grain structures in solidification processes [J]. Acta Metallurgica Materialia, 1994, 42(7): 2233−2246.

[13] GANDIN C A, RAPPAZ M. A 3D cellular automaton algorithm for the prediction of dendritic grain growth [J]. Acta Materialia, 1997, 45(5): 2187−2195.

[14] TSAI D C, HWANG W S. Numerical simulation of solidification morphologies of Cu−0.6Cr casting alloy using modified cellular automaton model [J]. Transactions of Nonferrous Metals Society of China, 2010, 20(6): 1072−1077.

[15] TSAI D C, HSU M S, HWANG W S, JIANG C S. Mathematical modeling of solidification microstructure of pure copper by vacuum continuous casting and its experimental verification [J]. ISIJ International, 2010, 50: 1843−1850.

[16] LUO Sen, ZHU Miao-yong, LOUHENKILPI S. Numerical simulation of solidification structure of high carbon steel in continuous casting using cellular automaton method [J]. ISIJ International, 2012, 52: 823−830.

[17] HOU Zi-bing, JIANG Fang, CHENG Guo-guang. Solidification structure and compactness degree of central equiaxed grain zone in continuous casting billet using cellular automaton-finite element method [J]. ISIJ International, 2012, 52(7): 1301−1309.

[18] ZHANG Zheng-xian, HUANG Fang, ZHANG Yan. Effects of micro-parameter on solidification structure of ZG12MnMoV low-alloy steel based on CAFE model [J]. Journal of Chongqing University (English Edition), 2016, 15(3): 111−118.

[19] LI Yang, SHTERENLIKHT A, REN Xiao-bo, HE Jian-ying, ZHANG Zhi-liang. CAFE based multi-scale modelling of ductile-to-brittle transition of steel with a temperature dependent effective surface energy [J]. Materials Science and Engineering: A, 2019, 755: 220−230.

[20] ABBASI M, BAGHERI B, SHARIFI F. Simulation and experimental study of dynamic recrystallization process during friction stir vibration welding of magnesium alloys [J]. Transactions of Nonferrous Metals Society of China, 2021, 31: 2626−2650.

[21] CAO zhuo-han, ZHOU Chen, WAN Zhi-peng, YANG Wen-hua, REN Li-li, HU Lian-xi. Cellular automaton simulation of dynamic recrystallization behavior in V−10Cr−5Ti alloy under hot deformation conditions [J]. Transactions of Nonferrous Metals Society of China, 2019, 29: 98−111.

[22] LU Wen-jian, XING Hui, HU Rui, ZHANG Qing-yu, YAO Zheng-jun. The effect of wettability on gas porosity formation during directional solidification of alloys: Insights from lattice Boltzmann-cellular automata simulations [J]. Journal of Materials Research and Technology, 2023, 22: 424−431.

[23] SUI Da-shan, SHAN Yu, WANG Dong-xin, LI Jun-yi, XIE Yao, YANG Yi-qun, DONG An-ping, SUN Bao-de. Elastic-viscoplastic constitutive equations of K439B superalloy and thermal stress simulation during casting process [J]. China Foundry, 2023, 20(5): 403−413.

[24] KURZ W, GIOVANOLA B, TRIVEDI R. Theory of microstructural development during rapid solidification [J]. Acta Metallurgica, 1986, 34(5): 823−830.

[25] GAO Shuang, SONG Zhen-feng, HE Bo, ZHOU Lan-zhang, HOU Jie-shan. Effect of Ta addition on solidification microstructure and element segregation of IN617B nickel-base superalloy [J]. Transactions of Nonferrous Metals Society of China, 2022, 32: 559−568.

[26] WANG Kai-meng, JING Hong-yang, XU Lian-yong, ZHAO Lei, HAN Yong-dian, LI Hai-zhou, SONG Kai. Microstructure evolution of 55Ni−23Cr−13Co nickel-based superalloy during high-temperature cyclic deformation [J]. Transactions of Nonferrous Metals Society of China, 2021, 31: 3452−3468.

[27] SHAN Yu, SUI Da-shan, Ma Jin-yuan, DONG An-ping, SUN Bao-de. Numerical simulation and experimental verification of microstructure evolution for K439B nickel-based superalloy in investment casting process [J]. Chinese Journal of Rare Metals, 2023, 47(7): 923−933. (in Chinese)

[28] LIU Gang, LIU Lin, LIU Xin-wang, WANG Zhi-jun, HAN Zhen-hua, ZHANG Guo-jun, KOSTKA A. Microstructure and mechanical properties of Al0.7CoCrFeNi high-entropy-alloy prepared by directional solidification [J]. Intermetallics, 2018, 93: 93−100.

基于实验与模拟方法的 K439B 镍基高温合金变截面铸件的显微组织演变

隋大山[1]，周德鹏[1]，刘 阳[1]，鄯 宇[1]，董安平[2]

1. 上海交通大学 材料科学与工程学院 塑性成形技术与装备研究院，上海 200030；
2. 上海交通大学 材料科学与工程学院 上海市先进高温材料与精密成形重点实验室，上海 200240

摘 要：为了揭示 K439B 镍基高温合金变截面铸件在重力精密铸造过程的显微组织演化特征，采用铸造实验和宏微观数值建模相结合的方法开展系统的研究。首先，对 K439B 合金变截面铸件进行了铸造实验，获得了铸件变截面部位的 SEM 和 EBSD 等显微组织形貌。然后，通过相图计算和 DSC 测试等方法确定了 K439B 合金的宏微观模拟参数，采用有限元与元胞自动机相结合的方法(CAFE)对 K439B 变截面铸件精密铸造过程进行了宏微观数值模拟。实验结果表明，随着截面比值的增加，平均晶粒面积由截面边缘到心部的比值呈增加趋势。模拟结果表明，随着截面比值由 6∶1 增大到 12∶1，平均晶粒面积由 0.885 mm^2 增至 0.956 mm^2。综合实验和模拟结果可知，铸件截面比值越大，晶粒大小越不均匀，晶粒形状也越不规则。CAFE 宏微观建模是模拟 K439B 合金显微组织演变的有效方法，能够保证模拟结果的精确度。

关键词：K439B 镍基高温合金；元胞自动机；元胞自动机有限元法；变截面；精密铸造；显微组织演变

(Edited by Wei-ping CHEN)